Article

Discovery Medicine 2025; 37(196): 933–945
https://doi.org/10.24976/Discov.Med.202537196.83

Nesfatin-1 Suppresses Inflammation in Bronchopulmonary Dysplasia by Regulating HMGB-1/TLR4/p65/NLRP3 Signaling Pathway

Xiaoting Yang[1], Gang Luo[2], Feifeng Lou[3,*]

[1]School of Medicine, Quzhou College of Technology, 324000 Quzhou, Zhejiang, China
[2]Department of Pharmacy, Jiangshan Hospital of Traditional Chinese Medicine, 324100 Quzhou, Zhejiang, China
[3]Department of Neonatal Pediatrics, Zhuji People's Hospital, 311800 Zhuji, Zhejiang, China
*Correspondence: nancyloufeifeng@sina.com (Feifeng Lou)
Published: 20 May 2025

Background: Bronchopulmonary dysplasia (BPD) is a common respiratory disease in premature infants. Nesfatin-1 is considered for the treatment of BPD. This study aimed to explore the anti-inflammatory effect of nesfatin-1 in the treatment of BPD.
Methods: Hyperoxia-induced newborn rats and transfected primary type II alveolar epithelial cells (AECIIs) were used to evaluate nesfatin-1's efficacy in treating BPD. Lung damage was assessed by means of wet-dry ratio measurement, Hematoxylin and Eosin staining, Masson staining, Terminal deoxynucleotidyl transferase-mediated dUTP nick-end labeling (TUNEL) staining, and Western blotting. Interleukin 6 (*Il-6*), tumor necrosis factor alpha (*Tnf-*α), and interleukin 1β (*Il-1*β) levels were measured by Enzyme-linked immunosorbent assay (ELISA) and quantitative polymerase chain reaction (qPCR). Neutrophils in bronchoalveolar lavage fluid were counted. High mobility group box 1 (HMGB-1), Toll-like receptor 4 (TLR4), nuclear factor kappa-light-chain-enhancer of activated B cells p65 subunit (p65), and NOD-like receptor family pyrin domain containing 3 (NLRP3) expressions were analyzed using Western blotting, while NLRP3 expression was detected through immunohistochemistry. AECIIs' viability, apoptosis, and reactive oxygen species (ROS) levels were assessed using cell counting kit-8 (CCK8), flow cytometry, and immunofluorescence, respectively. An immunofluorescence approach was used to detect surfactant protein C and ROS levels.
Results: *In vivo*, nesfatin-1 treatment significantly reduced the lung wet-dry ratio, increased the body weight of rats, inhibited apoptosis, alleviated lung damage, decreased inflammation, and lowered neutrophil counts ($p < 0.05$). *In vitro*, nesfatin-1 enhanced cell viability, inhibited apoptosis, decreased ROS levels ($p < 0.01$) and decreased mRNA levels of *Il-6*, *Tnf-*α, and *Il-1*β ($p < 0.05$) while increasing *Il-10* mRNA ($p < 0.01$). In *in vivo* and *in vitro* scenarios, nesfatin-1 inhibited HMGB-1, TLR4, p65, and NLRP3 protein expression ($p < 0.05$). In hyperoxia cells, *Hmgb-1* silencing showed similar results to those of nesfatin-1 treatment, while *Hmgb-1* overexpression antagonized the effects of nesfatin-1 treatment.
Conclusion: This study showed that nesfatin-1 reduces neutrophils and suppresses inflammation via the HMGB-1/TLR4/Nuclear Factor kappa-light-chain-enhancer of activated B cells (NF-κB)/NLRP3 pathway, suggesting its potential clinical application in the treatment of BPD.

Keywords: nesfatin-1; inflammation; high mobility group box 1; bronchopulmonary dysplasia

Introduction

Bronchopulmonary dysplasia (BPD) is a chronic respiratory disease commonly occurring in newborn infants, characterized by arrested lung development along with pulmonary fibrosis and airway injury [1]. Due to lung damage, newborn infants affected by BPD may suffer from complications such as pulmonary hypertension and respiratory infections, which can progress to asthma or chronic obstructive pulmonary disease and even lead to death [2]. Premature birth is the primary cause of BPD. Several studies have reported a dramatic elevation in the incidence and mortality of BPD in premature infants [3–5]. Thus, this urgently calls for the need to explore the pathogenesis of BPD and devise a therapeutic approach.

Apart from premature birth, the development of BPD was associated with other high-risk factors, such as preeclampsia [6], oxygen toxicity [7], and infection [8]. Particularly, mechanical ventilation and hyperoxia exposure induce the production of reactive oxygen species (ROS), ultimately leading to BPD [9]. In addition, immune response and inflammation induced by infection or ROS also play a vital role in BPD pathogenesis [10,11]. Therefore, counteracting inflammation provides another potential avenue for treating BPD.

High mobility group box 1 (HMGB-1) is a highly conserved nuclear protein involved in cell differentiation [12], migration [13], metastasis [14], and apoptosis [15]. Moreover, extracellular HMGB-1 can act as a damage-associated molecular pattern to activate the innate immune system and stimulate pro-inflammatory cytokine production [16].

Nesfatin-1, an 82-amino-acid peptide derived from the precursor protein nucleobindin 2 (NUCB2), has been reported to show antioxidant, anti-inflammatory and anti-apoptotic activities in multiple diseases [17]. Moreover, it has been reported to suppress macrophage M1 polarization to inhibit inflammation, thus reducing acute lung injury [18]. Furthermore, in our previous study, nefastin-1 has been proven to inhibit oxidative stress, protecting newborn mice from hyperoxia-induced lung injury [19].

In this study, we aimed to explore the therapeutic effect of nesfatin-1 on BPD by focusing on its anti-inflammatory properties, using a rat model of hyperoxia-induced BPD and type II alveolar epithelial cells (AECIIs).

Materials and Methods

Establishment of BPD Model in Neonatal Rats and Drug Administration

A total of 18 adult male and female rats (Specific Pathogen Free (SPF) grade, 200 ± 20 g, 6–8 weeks old) were purchased from SLAC Laboratory Animal Co. Ltd. (animal production license number: SCXK(Hu)2022-0004; Shanghai, China). The animals used in this study were maintained under specific pathogen-free conditions, a constant 12-hour light/dark cycle, a temperature maintained at 22 ± 2 °C, and humidity levels of 55–60%.

After one week of adaptive feeding, adult male and female Sprague-Dawley rats were housed in a 2:1 arrangement to facilitate natural intercourse. Pregnant rats naturally delivered their offspring at 21–22 days of gestation.

The rat model of BPD was established according to protocols described in a previous study [19]. In short, within the first 6 h after birth, newborn rats were randomly assigned to a control group, model group or nesfatin-1 group (n = 6 for each group). Neonatal rats in the control group were exposed to normal air, while those in the model and nesfatin-1 groups were exposed to 85% oxygen for 14 days. Exposure to hyperoxia was carried out in an organic glass chamber, where oxygen concentration was monitored by an oxygen controller and delivered by a solenoid valve. A daily 1-hour period was set aside for weighing and refilling of water and food.

After model construction, the rats in the control and model groups received subcutaneous injection with saline and those in the nesfatin-1 group received 20 µg/kg nesfatin-1 (HY-P71177, MCE, Princeton, NJ, USA) for seven consecutive days, respectively [19].

Lung Wet-Dry Ratio Detection

After 12 h of the last dose administered, the rats were euthanized through carbon dioxide inhalation and their lungs were obtained. The left lung was used for wet-dry ratio detection. Filter paper was used to clean the blood on the surface of the left lung and then its wet weight was determined, followed by the dry weight measurement after baking the lung sample at 80 °C for 48 h. The wet-dry ratio was defined as the ratio of lung wet weight to its dry weight.

Hematoxylin and Eosin Staining

The lung sample was collected, rinsed, fixed, dehydrated, embedded and then cut into sections. After roasting and dewaxing, the sections were hydrated and stained with hematoxylin (H3136, Sigma-Aldrich, St. Louis, MO, USA) for 3 min and differentiated for 15 s. The sections were then rinsed with water and bluing buffer (Bry-0001-04, Runnerbio Technology, Shanghai, China) for 15 s and stained with eosin Y (E4009, Sigma-Aldrich) for 3 min. Images were captured using a microscope (Nikon Eclipse Ci-L, Nikon, Tokyo, Japan).

Masson Staining

The section was sliced and dewaxed as mentioned above. The section was first stained with hematoxylin for 10 min, followed by 1% hydrochloric acid alcohol. Subsequently, Ponceau S (71033761, Sinopharm Chemical Reagent, Shanghai, China) and acid fuchsin (71033760, Sinopharm Chemical Reagent) were used for staining for 5 min, followed by a 3-minute phosphomolybdic acid staining for decolorization and then 1-minute aniline blue staining (71003644, Sinopharm Chemical Reagent). After the sections were dehydrated with ethanol and xylene, they were sealed with neutral resin and observed under a microscope (Nikon Eclipse Ci-L, Nikon, Tokyo, Japan). Collagen volume fractions were quantified using ImageJ software (version 8.0; National Institutes of Health, Bethesda, MD, USA).

Terminal Deoxynucleotidyl Transferase-Mediated dUTP Nick-End Labeling (TUNEL) Staining

Sections were dewaxed, incubated with proteinase K (ST532, Beyotime, Shanghai, China) and 0.1% Triton X-100 (30188928, Sinopharm Chemical Reagent), followed by washing in phosphate-buffered saline (PBS), and then stained with the TUNEL apoptosis detection kit (C1090, Beyotime). Images were collected and counted using CaseViewer 2.4 software (3DHISTECH Ltd., Budapest, Hungary) and ImageJ to count the positive (red) and total (blue) cells in each sample. The positive cell rate was determined by calculating the ratio of the number of positive cells to the number of total cells.

Western Blotting

Lung tissue samples (100 mg each) were chopped and soaked in 1 mL cold lysis buffer. After low-temperature homogenization (3 times × 20 s), the homogenate was placed in an ice bath for 15 min to complete the lysis process. The cell sample was discarded from the supernatant and washed twice with PBS to collect the cells. Then the sample was centrifuged at 1000 ×g for 5 min, after removing the supernatant, adding 600 µL of Radioimmunoprecipitation Assay (RIPA) lysate (P0013B, Beyotime) to the sample, and lysing on ice for 30 min. The homogenate or cell sample was centrifuged at 6000 ×g and 4 °C for 5 min, and the supernatant was transferred for concentration measurement using a Bicinchoninic Acid (BCA) kit (P0012, Beyotime).

Subsequently, a quarter volume of loading buffer was added to the sample, followed by heating in boiling water for 5 min and cooling at room temperature to denature the protein. The sample was stored at –20 °C for further study.

After the protein sample was run in Sodium Dodecyl Sulfate Polyacrylamide Gel Electrophoresis (SDS-PAGE) and transferred to a Polyvinylidene Fluoride membrane (PVDF) (10600023, GE Healthcare Life Sciences, Waltham, MA, USA), the protein sample was sealed with 5% skim milk for 2 h. Subsequently, the sample was incubated with the corresponding primary antibody at 4 °C overnight. On the next day, the sample was incubated with anti-rabbit Immunoglobulin G (IgG), Horseradish Peroxidase (HRP)-linked secondary antibody. The protein strips were observed using enhanced chemiluminescence (610020-9Q, Clinx, Shanghai, China) and quantified using ImageJ software.

The antibodies used are as follow: Bcl-2 Associated X protein (BAX) Antibody (AF0120, Affinity, Cincinnati, OH, USA; 1:1000); B-cell lymphoma 2 (BCL-2) Antibody (AF6139, Affinity; 1:1000); HMGB-1 Antibody (10829-1-AP, Proteintechm, Wuhan, China; 1:1000); Toll-like receptor 4 (TLR4) Antibody (AF7017, Affinity; 1:1000); nuclear factor kappa-light-chain-enhancer of activated B cells p65 subunit (p65) Antibody (AF5006, Affinity; 1:1000); NOD-like receptor family pyrin domain containing 3 (NLRP3) Antibody (DF7438, Affinity; 1:1000); Anti-rabbit IgG, HRP-linked Antibody (7074, CST, Danvers, MA, USA; 1:6000); β-actin Antibody (1115-1-RR, Proteintech; 1:10,000); and glyceraldehyde-3-phosphate dehydrogenase (GAPDH) Antibody (10494-1-AP, Proteintech; 1:10,000).

Bronchoalveolar Lavage Fluid Collection and Cell Count

Bronchoalveolar lavage fluid (BALF) was collected as previous study [20]. Briefly, the rats were lavaged with PBS post-euthanasia to obtain BALF. Then, the BALF was centrifuged at 1200 ×g for 10 min. Afterwards, the supernatant was dropped at the end of a clean, grease-free slide and then made into a cell smear, which was then left to dry without heating. The smear was stained according to the instructions, followed by washing with distilled water for 30 s, and counted under the microscope.

Enzyme-Linked Immunosorbent Assay (ELISA)

The BALF collected was centrifuged at 1200 ×g for 10 min to obtain supernatant. Separately, the blood sample was left to coagulate naturally at room temperature for 20 min, followed by centrifuging at 3500 ×g for 15 min to obtain serum. The lung tissue was pre-treated with pre-cooled PBS to remove residual blood. Then, the tissue was ground and homogenized on ice, followed by centrifugation at 6000 ×g for 5 min. Absorbance (Optical Density (OD)) of each well was measured at 450 nm using a microplate reader (CMaxPlus, Molecular Devices LLC., San Jose, CA, USA).

Then, the levels of interleukin 6 (IL-6), tumor necrosis factor alpha (TNF-α), and interleukin 1β (IL-1β) in rat serum, lung, and BALF were assessed using corresponding ELISA kits according to instructions. The kits used are as follows: IL-6 ELISA kit (ml064292, Mlbio, Shanghai, China), TNF-α ELISA kit (ml002859, Mlbio), and IL-1β ELISA kit (ml037361, Mlbio).

Immunohistochemistry

The section was dewaxed and incubated in 100 µL hydrogen peroxide blocking solution for 10 min. After washing, the section was soaked in Tris-Ethylenediaminetetraacetic acid (EDTA) (pH = 9.0) and boiled for 15 min, and then left to cool down naturally for 15 min.

One hundred microliters of 5% bovine serum albumin (BSA) solution were added to the section, followed by a 20-minute incubation. NLRP3 Antibody (DF7438, Affinity; 1:200) was added for an overnight incubation at 4 °C. Goat Anti-Rabbit IgG H&L (HRP) (ab97080, Abcam, Cambridge, UK; 1:5000) was added for a 30-minute incubation at 37 °C. The section was then stained with 3,3-diaminobenzidine tetrahydrochloride (DAB) (36203ES01, Yeasen, Shanghai, China) and counterstained with hematoxylin for 30 s. Subsequently, the section was differentiated with hydrochloric acid-alcohol for 1 s, and then allowed to wash in running tap water for 10 min. After dehydration, transparency, and sealing, the slide was observed under a microscope. Image-Pro Plus 6.0 software (Media Cybernetics, Rockville, MD, USA) was used to analyze the optical density and area of images. The average optical density (AOD) is calculated as the integral optical density/the area, which was used for statistical analysis.

Extraction and Culture of Primary AECIIs From Newborn Rats

After the newborn rats were euthanized by CO_2 inhalation, they were soaked in 75% ethanol. Subsequently, both lungs were carefully removed from each animal and

Table 1. Primer sequences.

Gene	Forward Primer (5′–3′)	Reverse Primer (5′–3′)
Hmgb-1	AGGCTTTTCCCCATTAACAACAC	CCCCTCCTTCCACCTTTCTAC
Gapdh	CTCAGTTGCTGAGGAGTCCC	ATTCGAGAGAAGGGAGGGCT
Il-6	CCACGGCCTTCCCTACTTC	TTGGGAGTGGTATCCTCTGTGA
Il-10	CATTCCATCCGGGGTGACAA	TTCTTCACCTGCTCCACTGC
Tnf-α	ATCCGAGATGTGGAACTGGC	CGATCACCCCGAAGTTCAGT
Il-1β	GACTTCACCATGGAACCCGT	GGAGACTGCCCATTCTCGAC
β-Actin	ATTGGTGGCTCTATCCTGGC	AAACGCAGCTCAGTAACAGTC

Hmgb-1, High mobility group box 1; *Gapdh*, glyceraldehyde-3-phosphate dehydrogenase; *Il-6*, interleukin 6; *Il-10*, interleukin 10; *Tnf-α*, tumor necrosis factor alpha; *Il-1β*, interleukin 1β.

washed twice in PBS to remove residual non-lung tissue and blood. The lung tissue was then cut into small pieces. Afterwards, the tissue pieces were incubated in 0.25% trypsin solution (GNM25200-1, JingKeBio, Hangzhou, China) at 37 °C for 45 min. During this time, the mixture was gently stirred every 10 minutes to ensure thorough digestion.

The reaction of trypsin was terminated by adding complete medium, and then, the tissue-reagent mixture was filtered through 200 mesh sieves to remove undigested lung tissue, followed by centrifugation at 1000 ×g for 3 min and supernatant removal. Dulbecco's Modified Eagle Medium (DMEM)/F12 complete medium was added to the pellets; after being resuspended, the sample was transferred for subsequent culture.

The cells were cultured in DMEM/F12 medium (iCell-000, iCell Bioscience, Shanghai, China), containing 10% fetal bovine serum and 1% penicillin-streptomycin, under the conditions of 5% CO_2, 37 °C and 80% humidity. After a certain period of culture, cell morphology was observed under a microscope to identify AECIIs, and quantitative polymerase chain reaction (qPCR) was employed to detect mycoplasma contamination.

AECIIs Transfection, Verification and Hyperoxia-Induced BPD Modeling

The 1×10^5/mL AECIIs were first seeded into 6-well culture plates with 2 mL medium and then transfected with an shRNA (Genepharma) or HEGB-1-targeting plasmid (Genepharma) and relevant negative control (sh-NC or oe-NC) by incubating with Lipofectamine TM3000 (L3000-008, Invitrogen, Waltham, CA, USA) for 48 h when the cell confluence reached 70%, followed by Western blotting and qPCR assays for verifying transfection efficacy.

To construct a hyperoxia injury model, the transfected AECIIs were exposed to 85% oxygen for 24 h. The cells were divided into control, model (hyperoxia exposure), nesfatin-1, *Hmgb-1* overexpression (oe-HMGB-1), oe-HMGB-1+nesfatin-1, and shRNA *Hmgb-1* (sh-HMGB-1) groups, which were labeled A–F, respectively.

Immunofluorescent Staining

AECIIs were fixed in 4% paraformaldehyde for 30 min at 37 °C. After permeabilization with 0.5% Triton X-100 at room temperature and blocking with 3% BSA for 30 min, cells were stained with surfactant protein C (SP-C) primary antibody (DF6647, Affinity, 1:200) at 4 °C overnight. Cells were then incubated with goat anti-rabbit Alexa Fluor® 647 secondary antibody (AB150080, Abcam, 1:500), followed by staining of nuclei with 4,6-diamidino-2-phenylindole (DAPI) for 5–10 min at room temperature. Images were acquired using a fluorescence microscope (Ts2-FC, Nikon, Tokyo, Japan). For the detection of ROS, immunofluorescence was performed using an ROS detection kit (S0033M, Beyotime). ImageJ software (National Institutes of Health) was used to analyze the proportion of SP-C positive cells in the total cell count and the mean fluorescence intensity (MFI) of 2,7-dichlorofluorescein (DCF), which is indicative of ROS activity.

Quantitative Polymerase Chain Reaction

Cells were collected and washed with PBS. The total RNA was extracted from samples using a special kit (AG21024, AmyJet, Wuhan, China) according to instructions. The Roche LightCycler 96 real-time fluorescence quantitative PCR instrument (LightCycler® 96, Roche, Basel, Switzerland) was used for qPCR. Reverse transcription was performed at 42 °C for 15 min; 85 °C for 5 min, followed by PCR at 95 °C denaturation for 10 min, 40 cycles at 95 °C for 15 s, and 60 °C for 60 s. Relative gene expression was estimated using the $2^{-\Delta\Delta CT}$ method as reported by Tang *et al.* [21]. Primer sequences are presented in Table 1.

Cell Counting Kit-8 (CCK8) Assay

Transfected AECIIs in the logarithmic growth phase were collected and then digested with 0.25% trypsin solution. After cell counting, the cells were added to serum-free culture medium to prepare a cell suspension (1.5×10^4/100 μL). Next, they were seeded into 96-well plates for overnight culture. AECIIs were modeled and/or treated

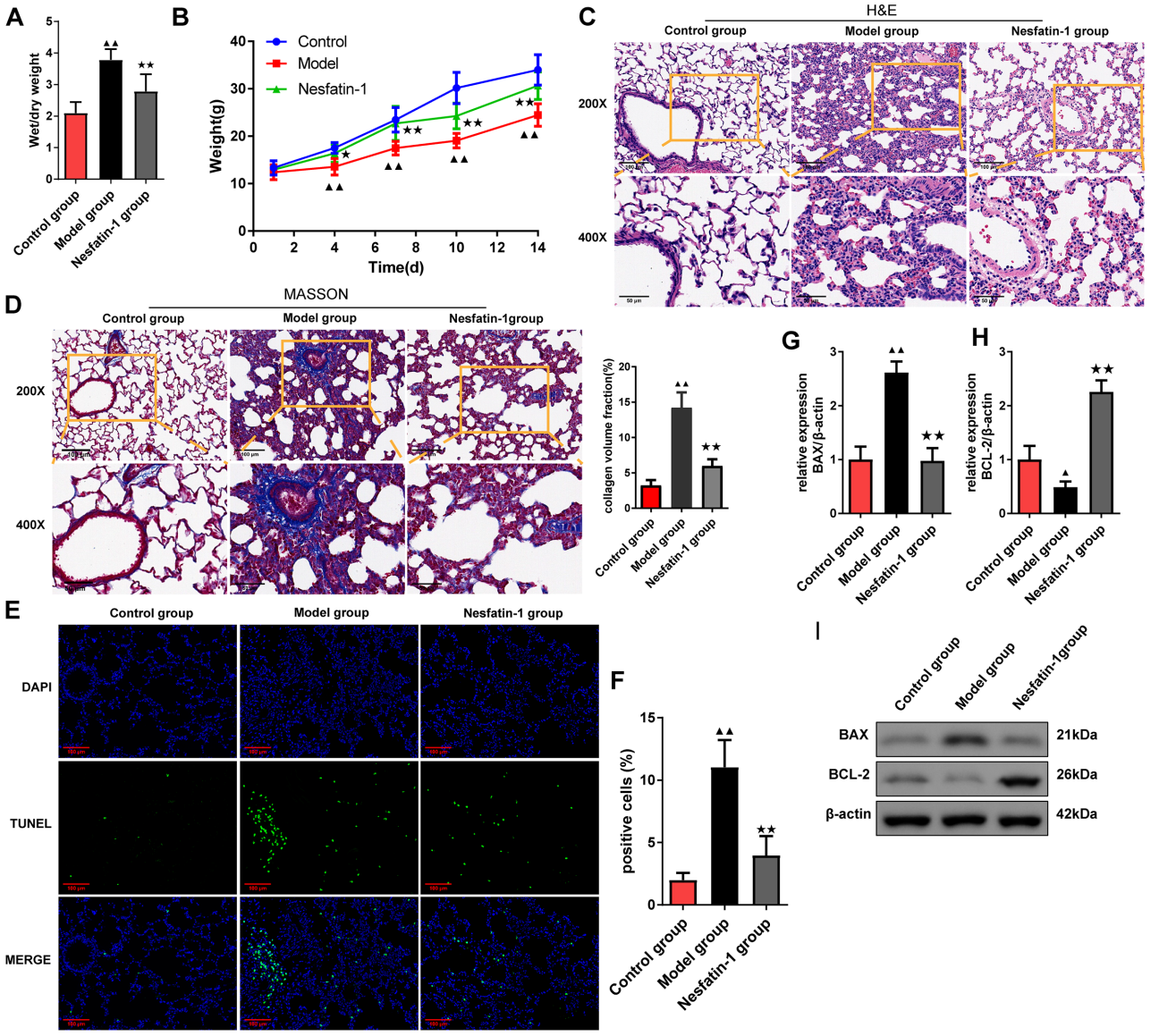

Fig. 1. Observations of pulmonary pathology in rat lungs. (A) The wet-dry ratio of the left lungs in each group (n = 6). (B) Body weight changes in rats (n = 6). (C) Hematoxylin and Eosin staining (n = 6); magnification: 200×, scale bar: 100 µm; magnification: 400×, scale bar: 50 µm. (D) Masson staining (n = 6); magnification: 200×, scale bar: 100 µm; magnification: 400×, scale bar: 50 µm. (E) TUNEL staining for dead cells in rat lungs; magnification: 200×, scale bar: 100 µm. (F) Positive dead cell percentage (n = 6). (G,H) The relative expression of Bcl-2 Associated X protein (BAX) (G) and B-cell lymphoma 2 (BCL-2) (H). (I) Western blot results (n = 3). $^{\blacktriangle}p < 0.05$, $^{\blacktriangle\blacktriangle}p < 0.01$ vs control group; $^{\bigstar}p < 0.05$, $^{\bigstar\bigstar}p < 0.01$ vs model group. DAPI, 4,6-diamidino-2-phenylindole; TUNEL, Terminal deoxynucleotidyl transferase-mediated dUTP nick-end labeling.

with nesfatin-1 according to group design for 24 h, followed by cell viability measurement using a CCK8 kit (C0039, Beyotime). OD of each well in the CCK8 assay was measured at 450 nm using a microplate reader (CMaxPlus). Cell viability was calculated using the following formula: (Optical Density (OD)) value of experimental group – OD value of blank) / (OD value of control group – OD value of blank) × 100%.

Cell Apoptosis Assay

In the cell apoptosis assay, 2 mL of cells (1.2 × 10^6 cells/well) were seeded into the 6-well plate for 24 h. Afterwards, the cells were collected, washed twice with precooled PBS, and resuspended to 1 × 10^6 cells/mL. After the addition of 500 µL binding buffer, the cell suspension was centrifuged. The supernatant was discarded, and 100 µL buffer was added to the pellet prior to mixing. Then, apoptosis was detected using an apoptosis kit (556547, BD, Franklin Lakes, NJ, USA). In short, 5 µL An-

nexin V-Fluorescein Isothiocyanate (FITC) and 10 µL Propidium Iodide (PI) were added, mixed, and then incubated for 15 min at room temperature in the dark. Following the addition of 400 µL of binding buffer, the apoptosis rate was detected using flow cytometry (NovoCyte, Agilent, Santa Clara, CA, USA) within 1 h. The experiment was repeated 3 times.

Statistical Analysis

In the current study, data were analyzed by SPSS 20.0 (IBM Corp., Chicago, IL, USA). Data are expressed as mean ± standard error of mean. One-way analysis of variance (ANOVA) was used to analyze normally distributed data that satisfied the homogeneity of variance, and further two-by-two comparisons between groups were performed using Tukey's test. Dunnett's T3 test was used if the data were normally distributed, but did not meet the homogeneity of variance. Statistical threshold was set at $p < 0.05$.

Results

Nesfatin-1 Attenuates Lung Pathological Injury Induced by BPD

To assess the pathological change in the lung, we measured the lung wet-dry ratio and performed pathological staining. As shown in Fig. 1A, the wet-dry ratio was markedly elevated after BPD modeling ($p < 0.01$), indicating a severe BPD-induced pulmonary edema. On the contrary, nesfatin-1 treatment effectively reduced the wet-dry ratio of the lung ($p < 0.01$). The changes in the body weight of rats are shown in Fig. 1B. The body weight of rats in the model group was significantly lower ($p < 0.01$) on days 4–14 compared with the control group. The body weight of rats in the nesfatin-1 group was considerably higher ($p < 0.05$ or $p < 0.01$) on days 4–14 compared with the model group.

In addition, the Hematoxylin and Eosin staining results suggested that compared to the intact lung tissue in the control group, lung tissue in the model group exhibited severe inflammatory cell infiltration, in tandem with alveolar septa widening, along with the onset of edema and congestion. However, nesfatin-1 treatment resulted in the shrinkage of alveolar septa and mitigated inflammatory cell infiltration, edema, and congestion (Fig. 1C).

Moreover, Masson staining was used to assess fibrosis in the lung. As shown in Fig. 1D, a clear alveolar structure was observed in the control group, with a small amount of blue filamentous collagen fiber deposition seen at the edge of the alveoli. In contrast, a large amount of blue filamentous collagen fiber deposition in the alveolar wall tissue of the model group was observed, along with collapse, fusion, and widening of the alveolar septum. The alveolar structure in the nesfatin-1 group was relatively intact, with a reduction in blue fiber area and a thinning of alveolar spacing.

Furthermore, we performed TUNEL staining and measured biomarker expression to assess apoptosis in the lung tissue. As shown in Fig. 1E,F, compared to the positive cells in the control group, the dramatic increase in positive cells suggested a rise in cell apoptosis, which was alleviated by nesfatin-1 treatment ($p < 0.01$). Western blot results are shown in Fig. 1G–I. Compared to the control group, BAX expression was upregulated ($p < 0.01$), indicating an increase in apoptosis, while the BCL-2 expression decreased to a modest extent ($p < 0.05$) in the model group. Interestingly, the nesfatin-1 treatment notably reversed the BPD-induced apoptosis.

Nesfatin-1 Mitigates Lung Inflammation Activated by BPD

Subsequently, we measured inflammatory factors IL-6, TNF-α, and IL-1β in serum, lung tissue, and BALF to assess the degree of inflammation in rats. As shown in Fig. 2A–I, compared with the control group, the levels of IL-6, TNF-α, and IL-1β in serum, lung tissue, and BALF of rats in the model group were markedly elevated ($p < 0.01$); and the levels of IL-6, TNF-α, and IL-1β in serum, lung tissue, and BALF of rats in the nesfatin-1 group were notably reduced ($p < 0.01$) compared with those in the model group. Neutrophil count in rat BALF is presented in Fig. 2J. Compared with the control group, the number of neutrophils in rat BALF in the model group was dramatically raised ($p < 0.01$), whereas compared with the model group, the number of neutrophils in rat BALF in the nesfatin-1 group was dramatically decreased ($p < 0.01$). These findings collectively point to the potential of nesfatin-1 in suppressing BPD-induced inflammation.

Nesfatin-1 Inhibits the HMGB-1/TLR4/NLRP3 Pathway

To explore the mechanism behind the therapeutic potential of nesfatin-1 in BPD, we measured protein expression related to the HMGB-1/TLR4/NLRP3/Nuclear Factor kappa-light-chain-enhancer of activated B cells (NF-κB) pathway. As shown in Fig. 3A–E, the model group showed an increase in relative protein expression of HMGB-1, TLR4, p65, and NLRP3, which is suggestive of pathway activation ($p < 0.01$). In contrast, nesfatin-1 treatment decreased the expression of HMGB-1, TLR4, p65 and NLRP3 proteins ($p < 0.01$). Furthermore, the immunohistochemical staining (Fig. 3F,G) showed that compared to the control group, NLRP3 expression was remarkably elevated in the model group ($p < 0.01$), and compared to the model group, the nesfatin-1 group exhibited decreased NLRP3 expression after treatment ($p < 0.01$), indicating that nesfatin-1 can suppress the activation of inflammation-related signaling pathway.

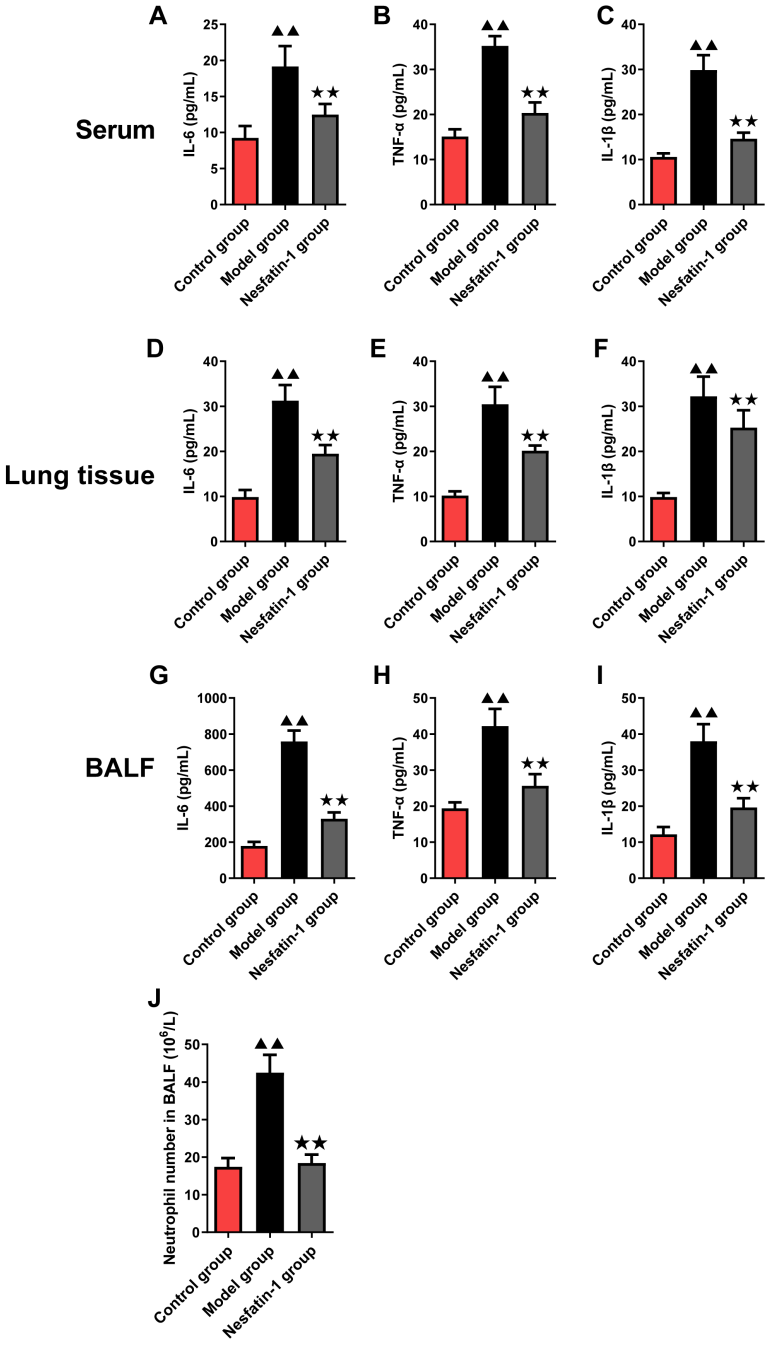

Fig. 2. Comparison of inflammatory factors and neutrophils. (A–C) The expression of IL-6 (A), TNF-α (B), and IL-1β (C) in serum (n = 6); (D–F) The expression of IL-6 (D), TNF-α (E), and IL-1β (F) in lung tissue (n = 6); (G–I) The expression of IL-6 (G), TNF-α (H), and IL-1β (I) in BALF (n = 6); (J) Neutrophil count in BALF (n = 6). $^{\blacktriangle\blacktriangle}p < 0.01$ vs control group; $^{\bigstar\bigstar}p < 0.01$ vs model group. Abbreviations: BALF, bronchoalveolar lavage fluid; IL, interleukin; TNF-α, tumor necrosis factor alpha.

AECIIs Identification and Transfection Efficiency Verification

The morphology of isolated cells was observed to determine AECIIs. As shown in Fig. 4A, we observed a large number of particles in the cytoplasm, in elliptical or short spindle-shaped cells with large, obvious nuclei, after a 24-hour culture. However, after 72 h of culture, the cell shape was notably enlarged, with the formation of a long spindle or irregular triangle. After passage, the cells transformed into polygonal shapes and interconnected to form cell monolayers, with plump cell bodies and clear cell edges. The qPCR results indicated that the AECIIs were not contaminated with mycoplasma (**Supplementary Fig. 1**). Then, the purity of AECIIs was detected by means of SP-C staining, and red fluorescence indicated SP-C-positive

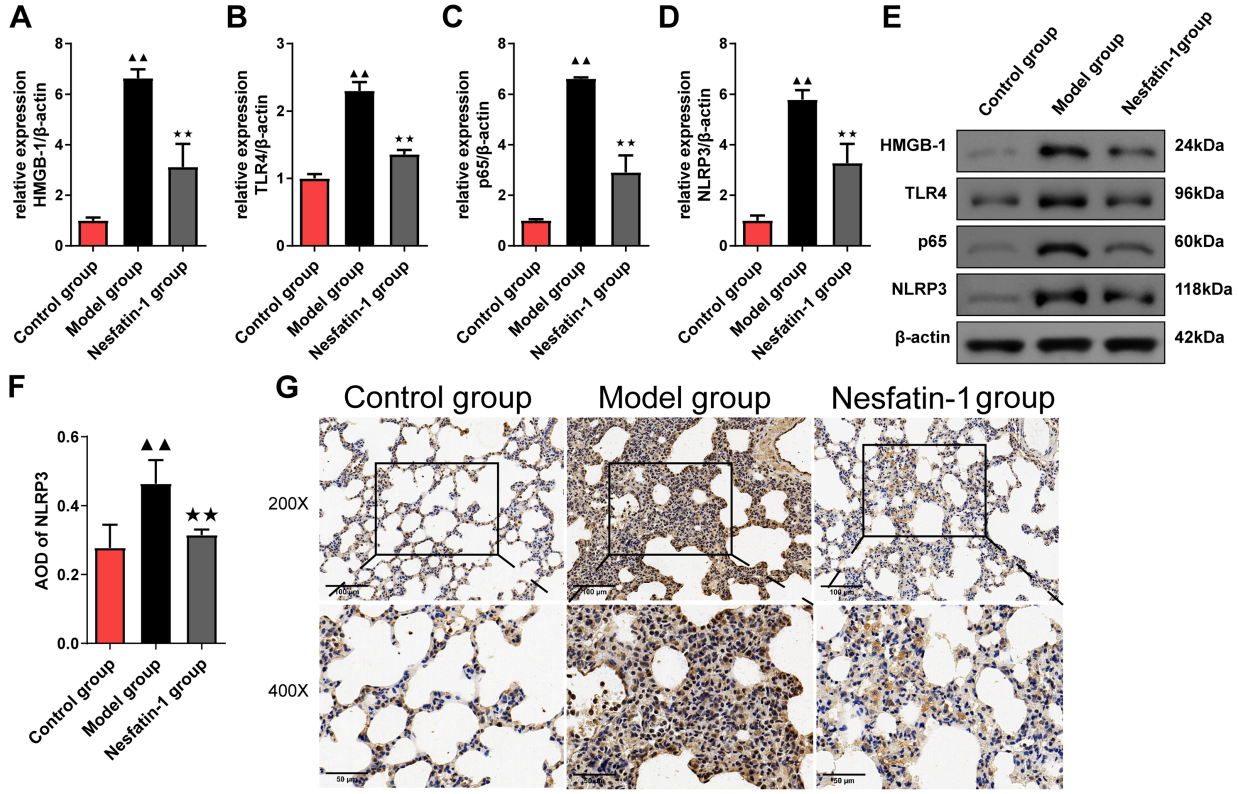

Fig. 3. Expression of relative protein of HMGB-1/TLR4/NLRP3 pathway. (A–D) Relative expression of HMGB-1 (A), TLR4 (B), p65 (C), and NLRP3 (D). (E) Western blot results of the proteins ($n = 3$). (F) For immunohistochemical analysis, the average optical density (AOD) of NLRP3 was calculated as the optical density/the area using Image-Pro Plus 6.0. (G) Representative immunohistochemical staining images of NLRP3 ($n = 6$); magnification: 200×, scale bar: 100 µm; magnification: 400×, scale bar: 50 µm. ▲▲$p < 0.01$ vs control group; ★★$p < 0.01$ vs model group. TLR4, Toll-like receptor 4; p65, nuclear factor kappa-light-chain-enhancer of activated B cells p65 subunit; NLRP3, NOD-like receptor family pyrin domain containing 3.

cells. Fig. 4B shows that the proportion of SP-C-positive cells is greater than 97%, indicating successful isolation of AECIIs.

Transfection efficiency was assessed using Western blotting and qPCR analysis. As shown in Fig. 4C,D, both protein and mRNA levels of *Hmgb-1* were notably elevated in the oe-HMGB-1 group compared to the oe-NC group but decreased in the sh-HMGB-1 group compared to the sh-NC group ($p < 0.01$), indicating successful transfection.

Subsequently, cell viability was detected with the CCK8 assay after *Hmgb-1* knockdown or overexpression. The results revealed that the cell viability of AECIIs cells in the overexpression of *Hmgb-1* group was dramatically reduced after 24- and 72-h culture compared to oe-NC group ($p < 0.01$) (Fig. 4E). Compared with sh-NC group, AECIIs cells in the *Hmgb-1* knockdown group exhibited a remarkable decrease in cell viability after a 24-h culture ($p < 0.05$) and a remarkable increase in cell viability after a 72-h culture ($p < 0.01$). These results indicated that sh-NC and oe-NC did not affect the viability of the control group, suggesting that *Hmgb-1* gene expression levels directly affect cell viability.

Nesfatin-1 Alleviates Hyperoxia-Induced Damage

The AECIIs morphology was observed for the purpose of verifying successful hyperoxia model construction. As shown in Fig. 5A, relative to the control group, exposure to hyperoxia resulted in changes in AECIIs morphology, partial cell shrinkage, decreased cell adhesion, and deteriorated cell function, indicating successful construction of a hyperoxia model.

Furthermore, to assess the influence of hyperoxia on AECIIs, cell viability was measured using the CCK8 assay and apoptosis was identified using flow cytometry. As illustrated in Fig. 5B–D, hyperoxia exposure significantly reduced the viability of AECIIs ($p < 0.01$). Interestingly, nesfatin-1 treatment can counteract the damage caused by hyperoxia. HMGB-1 silencing exhibited an anti-hyperoxia effect similar to the impact of nesfatin-1 ($p < 0.01$). In contrast, HMGB-1 overexpression exacerbated hyperoxia-induced damage, reversing the protective effect of nesfatin-1 ($p < 0.05$).

ROS staining, as shown in Fig. 5E,F, MFI of DCF indicates ROS activity. Compared with the control group, the MFI of DCF was greatly elevated in the model group

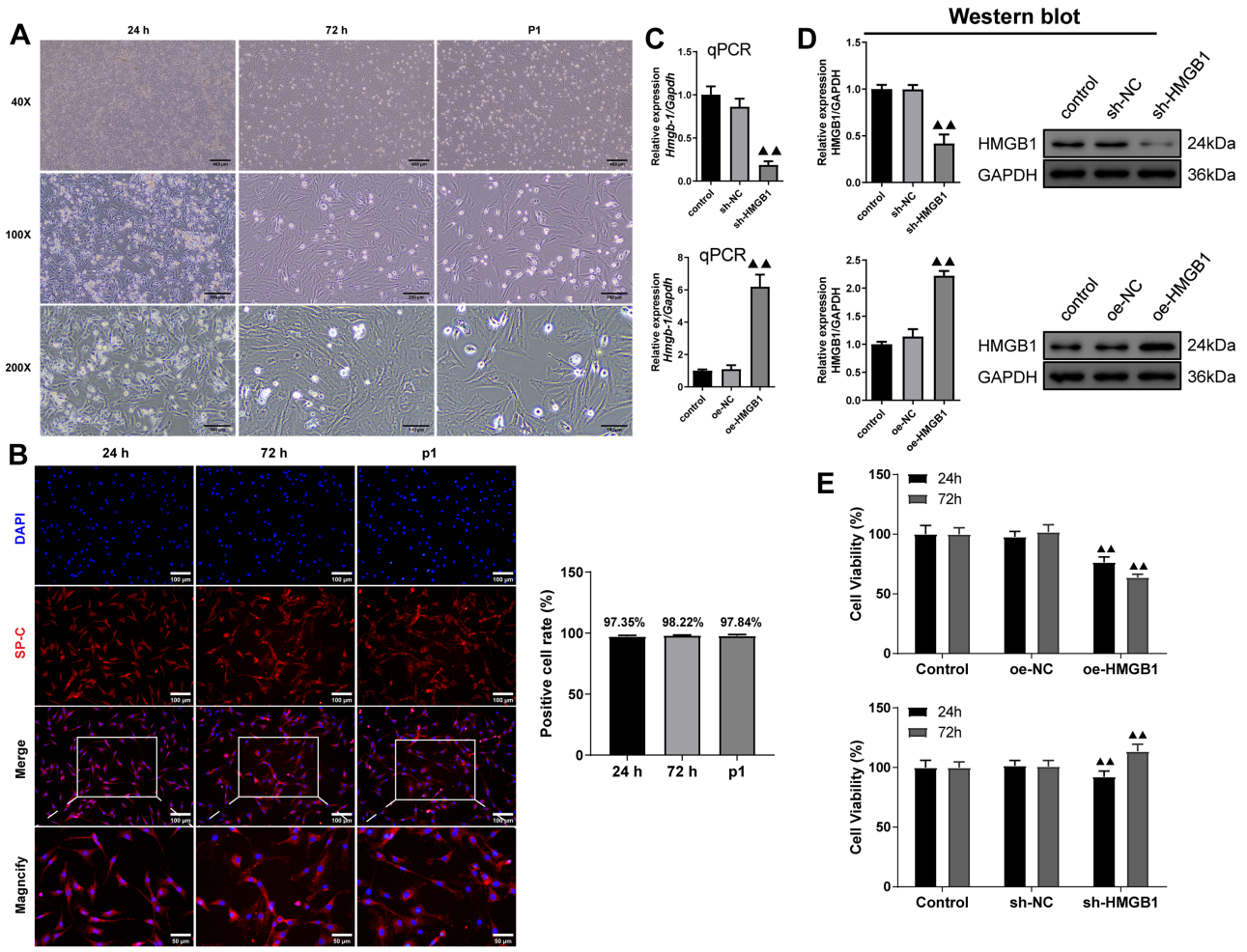

Fig. 4. Type II alveolar epithelial cells (AECIIs) identification and transfection verification. (A) Observation of cell morphology; magnification: 40×, scale bar: 400 µm; magnification: 100×, scale bar: 200 µm; magnification: 200×, scale bar: 100 µm. (B) The expression of SP-C in AECIIs cells at each time point (n = 3); magnification: 200×, scale bar: 100 µm; magnification: 400×, scale bar: 50 µm. (C) Relative expression of *Hmgb-1* mRNA was analyzed using quantitative polymerase chain reaction (qPCR) (n = 3). (D) Relative expression of HMGB-1 proteins was determined by means of Western blotting. Representative protein blot bands are shown (n = 3). (E) Determination of cell viability using CCK8 assay after overexpression or knockdown of *Hmgb-1* (n = 6). ▲▲$p < 0.01$ vs sh-NC or oe-NC group. Abbreviations: P1, First-passage cells; SP-C, Surfactant protein C; CCK8, cell counting kit-8.

($p < 0.01$); compared with the model group, the MFI of DCF was greatly reduced in the nesfatin-1 group and the HMGB-1 silencing group ($p < 0.01$), and the MFI of DCF in the HMGB-1 overexpression group was greatly elevated ($p < 0.01$); compared with the nesfatin-1 group, the MFI of DCF was significantly enhanced in the nesfatin-1+HMGB-1 overexpression group ($p < 0.01$). Therefore, we hypothesized that HMGB-1 was involved in hyperoxia-induced damage, which can be mitigated by nesfatin-1 by inhibiting HMGB-1.

Nesfatin-1 Inhibits the HMGB-1 Expression and Suppresses Secretion of Pro-Inflammatory Factors

Western blot results, as presented in Fig. 6A–E, show that the protein expression levels of HMGB-1, TLR4, p65, and NLRP3 were remarkably reduced in AECIIs in the nesfatin-1 group and the *Hmgb-1* silencing group compared to the model group ($p < 0.05$ or $p < 0.01$), and the protein expression levels of HMGB-1, TLR4, p65, and NLRP3 were markedly increased in the HMGB-1 overexpression group ($p < 0.01$). Compared with the nesfatin-1 group, HMGB-1, TLR4, p65, and NLRP3 protein expression levels were markedly increased in HMGB-1 overexpression+nesfatin-1 group ($p < 0.01$).

The qPCR results are shown in Fig. 6F–I. Compared with the control group, *Il-6*, *Tnf-α*, and *Il-1β* mRNA expression were conspicuously elevated ($p < 0.01$) and *Il-10* mRNA expression was conspicuously decreased ($p < 0.01$) in the model group. Compared with the model group, *Il-6*, *Tnf-α*, and *Il-1β* mRNA expression were markedly decreased ($p < 0.05$ or $p < 0.01$) and *Il-10* mRNA expression level was markedly increased ($p < 0.01$) in the nesfatin-1

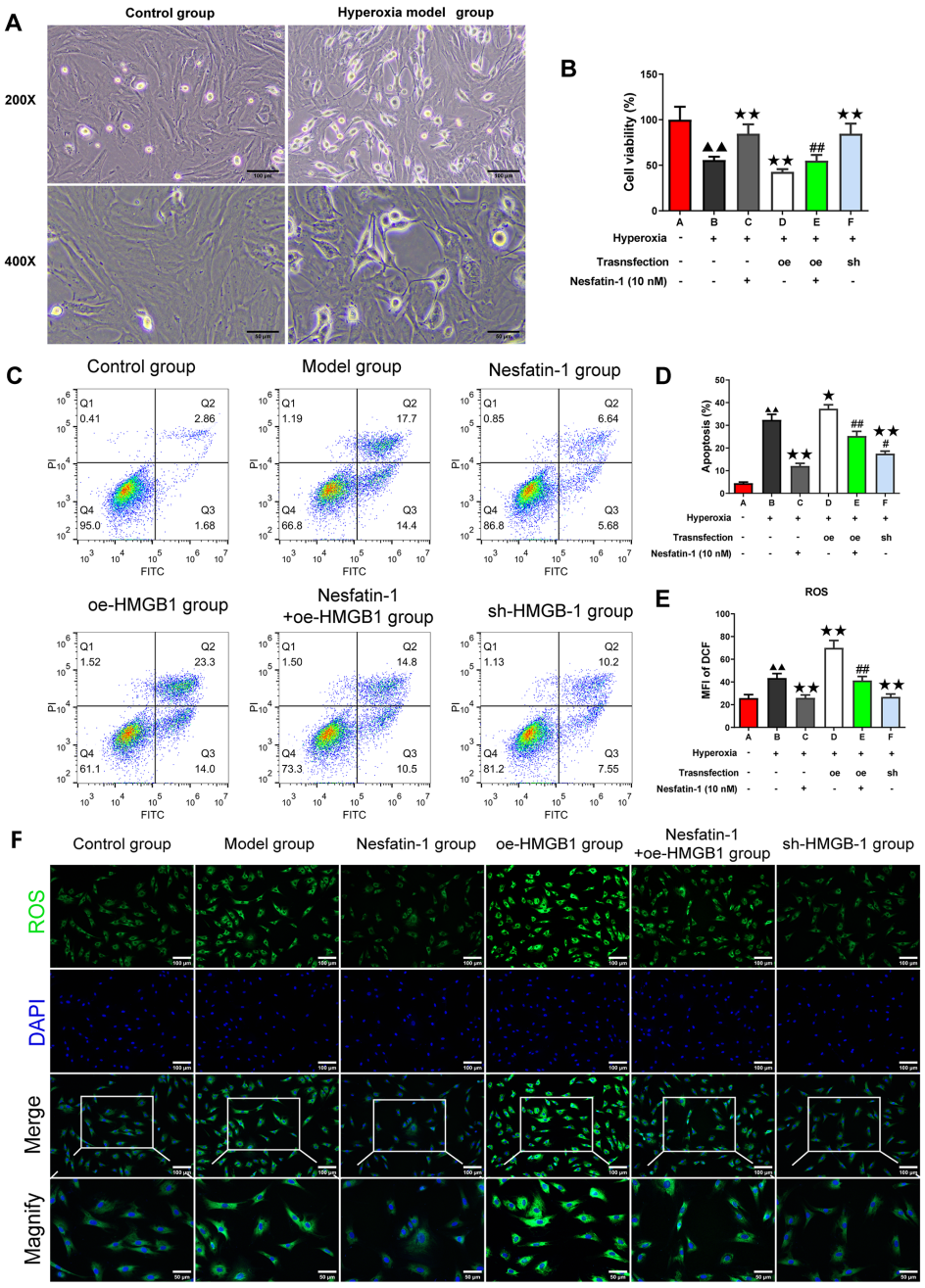

Fig. 5. Hyperoxia-induced damage in AECIIs. (A) Observation of cell morphology; magnification: 200×, scale bar: 100 μm; magnification: 400×, scale bar: 50 μm. (B) Cell viability ($n = 6$). (C) Detection of cell apoptosis by means of flow cytometry. The flow cytometry quadrant diagram was shown. (D) Quantitative results of cell apoptosis rate ($n = 3$); oe, plasmid transfection targeting HMGB-1; sh, shRNA transfection targeting HMGB-1. (E,F) The mean fluorescence intensity (MFI) of 2,7-dichlorofluorescein (DCF), which is indicative of reactive oxygen species (ROS) activity, was detected by immunofluorescence ($n = 3$); magnification: 200×, scale bar: 100 μm; magnification: 400×, scale bar: 50 μm. Groups A–F correspond to the control, model (hyperoxia exposure), nesfatin-1, oe-HMGB-1, oe-HMGB-1+nesfatin-1, and sh-HMGB-1 groups, respectively. $^{▲▲}p < 0.01$ vs control group; $^{★}p < 0.05$, $^{★★}p < 0.01$ vs model group; $^{\#}p < 0.05$, $^{\#\#}p < 0.01$ vs nesfatin-1 group.

group and the HMGB-1 silencing group. In the HMGB-1 overexpression group, mRNA expression level of *Il-6*, *Tnf-α* and *Il-1β* was obviously enhanced ($p < 0.05$ or $p < 0.01$), and the expression level of *Il-10* mRNA was markedly diminished ($p < 0.05$). Compared with the nesfatin-1 group, the expression levels of *Il-6*, *Tnf-α*, and *Il-1β* mRNA in the HMGB-1 overexpression+nesfatin-1 group were obviously elevated ($p < 0.05$ or $p < 0.01$), and the expression level of *Il-10* mRNA was markedly reduced ($p < 0.01$).

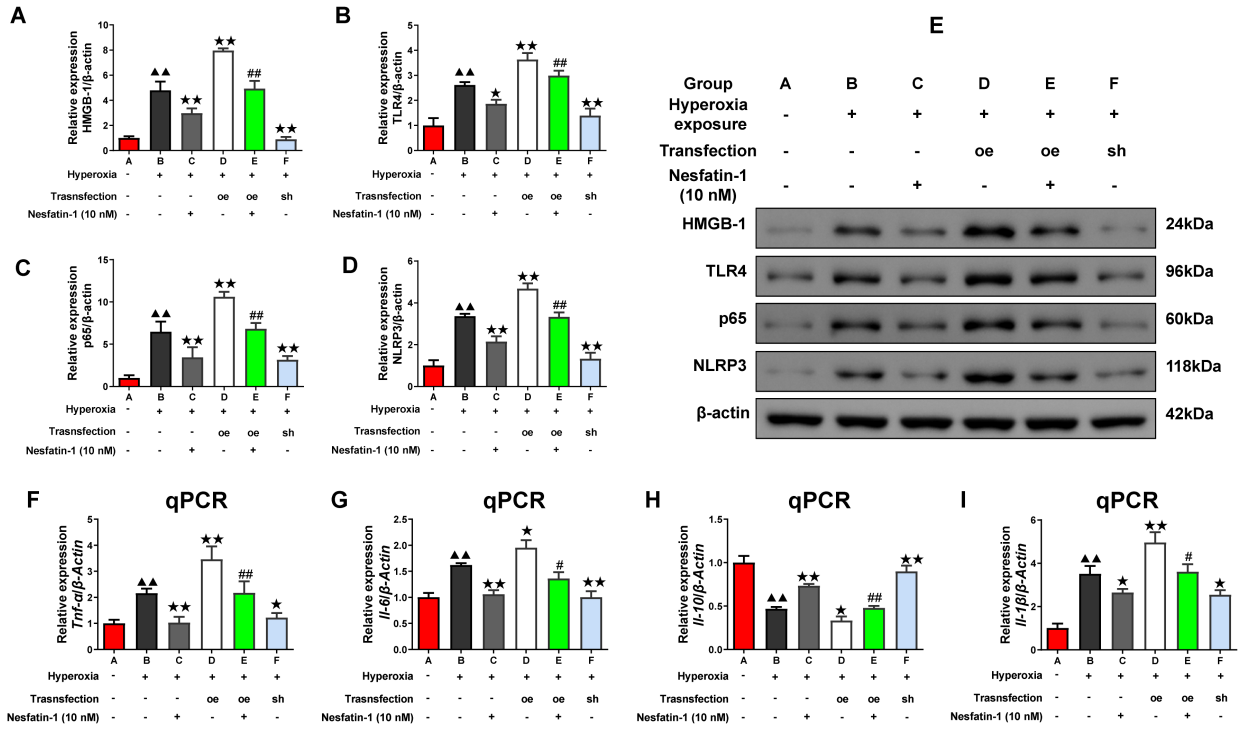

Fig. 6. Western blot assay of proteins related to HMGB-1/TLR4/NLRP3 pathway and mRNA expression of inflammatory factors. (A–D) The relative expression of HMGB-1 (A), TLR4 (B), p65 (C), and NLRP3 (D) ($n = 3$). (E) Western blot results. (F–I) The relative mRNA expression of *Tnf-α* (F), *Il-6* (G), *Il-10* (H), and *Il-1β* (I). $^{▲▲}p < 0.01$ vs control group; $^{★}p < 0.05$, $^{★★}p < 0.01$ vs model group; $^{\#}p < 0.05$, $^{\#\#}p < 0.01$ vs nesfatin-1 group.

Discussion

Our results demonstrated that nesfatin-1 can inhibit inflammation and alleviate hyperoxia-induced damage, in both *in vivo* and *in vitro* settings. Moreover, HMGB-1 overexpression aggravated hyperoxia-induced damage and counteracted the protective effect of nesfatin-1. These findings suggest that nesfatin-1 may potentially suppress inflammation by interfering with the HMGB-1/TLR4/NF-κB/NLRP3 signaling pathway, thereby alleviating BPD.

Hyperoxia exposure, possibly occurring during mechanical ventilation, was identified as a risk factor for the development of BPD [22]. Geetha *et al*. [23] reported that an individual might be facing a 5.5 times increased risk of BPD 7 days after mechanical ventilation. Their study provides a justification in this study to utilize hyperoxia exposure to construct a rat model of BPD. Moreover, the increasing wet-dry weight ratio of the lung and the pathological staining results revealed pulmonary edema, lung fibrosis, and apoptosis in lung tissue following hyperoxia exposure, which are consistent with the pathological characteristics of BPD.

As noted in previous studies, the risk factors for BPD are multifold. However, the inflammatory response is a key driver of distorted lung development [24,25]. Neutrophils, functioning as the primary cells of immunological defense, play a critical role in the onset and progression of acute lung injury [26,27]. However, excessive release of ROS and neutrophil extracellular traps by neutrophils may contribute to BPD development [28,29]. For example, Sun *et al*. [27] have reported that neutrophil extracellular traps caused BPD-like damage in neonatal mice via the WNT/β-catenin pathway. Similarly, we found a sharp increase in neutrophil count in BALF. Interestingly, nesfatin-1 treatment contributed to a significant reduction in the influx of neutrophils into the BALF. A study by Zhao *et al*. [30] reported that suppression of the HMGB-1/TLR4/p-38 MAPK/ROS axis may inhibit the formation of neutrophil extracellular traps in rats with hyperhomocysteinemia. Therefore, combined with their findings, our data suggest that nesfatin-1 reduces BPD damage by inhibiting neutrophil activation.

HMGB-1, an endogenous mediator of inflammation, can be secreted by immune cells and regulated via multiple biological processes, such as calcium signaling and ROS [30,31]. In addition, *in vivo* experiments have shown that HMGB-1 is implicated in the progression of reoxygenation damage [32].

Previous studies have also demonstrated that TLR4 can activate the NF-κB signaling pathway, followed by interaction with HMGB-1, resulting in NLRP3 inflammasome activation [33–35]. Our study showed that nesfatin-1 exerts an inhibitory effect on HMGB-1, thereby abrogating NLRP3 inflammasome activation both *in vivo* and *in vitro*.

It is well established that the activation of NLRP3 inflammasome is linked to the expression of inflammatory factors [36]. For instance, IL-1β and TNF-α expression can induce activation and expression of NLRP3 inflammasome.

The current study offers some preliminary insights into the potential value of nesfatin-1 in the treatment of BPD, but several limitations of the study should be acknowledged. Firstly, animal models inherently differ from human clinical samples, and thus, these findings require further validation through additional basic research and clinical trials. Secondly, our study did not assess the potential adverse effects of nesfatin-1 in animal models. Future preclinical investigations should carefully evaluate the safety profile of nesfatin-1 to inform its translational potential. Future studies will focus on the clinical translational applications of nesfatin-1, including optimization of the therapeutic dose, biosafety assessment, and development of targeted delivery systems.

Conclusion

In conclusion, nesfatin-1 can reduce neutrophil content and suppress inflammation, mitigating BPD-like characteristics in *in vitro* and *in vivo* scenarios. This protective effect is probably mediated through the regulation of the HMGB-1/TLR4/NF-κB/NLRP3 pathway. In summary, this study offers preliminary evidence on the therapeutic potential of nesfatin-1 in BPD treatment and reveals the potential mechanisms behind the compound's protective effect.

Availability of Data and Materials

The data used and/or analyzed during the current study are available from the corresponding author upon reasonable request.

Author Contributions

XY: Conceptualization, Data curation, Formal analysis, Investigation, Methodology, Project administration, Visualization, Writing-original draft. GL: Data curation, Formal analysis, Investigation, Methodology, Validation, Visualization, Writing-critical revision. FL: Conceptualization, Data curation, Methodology, Project administration, Supervision, Writing-critical revision. All authors have given final approval of the version to be published. All authors have participated sufficiently in the work to take public responsibility for appropriate portions of the content and agreed to be accountable for all aspects of the work in ensuring that questions related to its accuracy or integrity.

Ethics Approval and Consent to Participate

All animal experiments in this work were granted by the Animal Experimentation Ethics Committee of Hangzhou Hunter Youjian Biotechnology Center (Certificate No. SYXK(Zhe) 2024-0003) and conducted following the guidelines of the Institutional Animal Care and Use Committee (Approval number: IACUC/HTYJ-8201-17).

Acknowledgment

Not applicable.

Funding

This research received funding from Quzhou City Science and Technology Research Project (grant number 2023K240).

Conflict of Interest

The authors declare no conflict of interest.

Supplementary Material

Supplementary material associated with this article can be found, in the online version, at https://doi.org/10.24976/Discov.Med.202537196.83.

References

[1] Sikdar O, Harris C, Greenough A. Improving early diagnosis of bronchopulmonary dysplasia. Expert Review of Respiratory Medicine. 2024; 18: 283–294. https://doi.org/10.1080/17476348.2024.2367584.

[2] Homan TD, Nayak RP. Short- and Long-Term Complications of Bronchopulmonary Dysplasia. Respiratory Care. 2021; 66: 1618–1629. https://doi.org/10.4187/respcare.08401.

[3] Lee DMX, Tan AKS, Ng YPM, Amin Z. Quality of life of patients and caregivers affected by bronchopulmonary dysplasia: a systematic review. Quality of Life Research: an International Journal of Quality of Life Aspects of Treatment, Care and Rehabilitation. 2023; 32: 1859–1869. https://doi.org/10.1007/s11136-022-03311-y.

[4] Romijn M, Dhiman P, Finken MJJ, van Kaam AH, Katz TA, Rotteveel J, *et al*. Prediction Models for Bronchopulmonary Dysplasia in Preterm Infants: A Systematic Review and Meta-Analysis. The Journal of Pediatrics. 2023; 258: 113370. https://doi.org/10.1016/j.jpeds.2023.01.024.

[5] Principi N, Di Pietro GM, Esposito S. Bronchopulmonary dysplasia: clinical aspects and preventive and therapeutic strategies. Journal of Translational Medicine. 2018; 16: 36. https://doi.org/10.1186/s12967-018-1417-7.

[6] Tousty P, Fraszczyk-Tousty M, Ksel-Hryciów J, Łoniewska B, Tousty J, Dzidek S, *et al*. Adverse Neonatal Outcome of Pregnancies Complicated by Preeclampsia. Biomedicines. 2022; 10: 2048. https://doi.org/10.3390/biomedicines10082048.

[7] Behnke J, Dippel CM, Choi Y, Rekers L, Schmidt A, Lauer T, *et al*. Oxygen Toxicity to the Immature Lung-Part II: The Unmet Clinical Need for Causal Therapy. International Journal of Molecular Sciences. 2021; 22: 10694. https://doi.org/10.3390/ijms221910694.

[8] Bancalari E. Antenatal Infections and Respiratory Outcome in Preterm Infants. American Journal of Perinatology. 2020; 37: S39–S41. https://doi.org/10.1055/s-0040-1714347.

[9] Thomas JM, Sudhadevi T, Basa P, Ha AW, Natarajan V, Harijith A. The Role of Sphingolipid Signaling in Oxidative Lung

Injury and Pathogenesis of Bronchopulmonary Dysplasia. International Journal of Molecular Sciences. 2022; 23: 1254. https://doi.org/10.3390/ijms23031254.

[10] Salimi U, Dummula K, Tucker MH, Dela Cruz CS, Sampath V. Postnatal Sepsis and Bronchopulmonary Dysplasia in Premature Infants: Mechanistic Insights into "New BPD". American Journal of Respiratory Cell and Molecular Biology. 2022; 66: 137–145. https://doi.org/10.1165/rcmb.2021-0353PS.

[11] Perez M, Robbins ME, Revhaug C, Saugstad OD. Oxygen radical disease in the newborn, revisited: Oxidative stress and disease in the newborn period. Free Radical Biology & Medicine. 2019; 142: 61–72. https://doi.org/10.1016/j.freeradbiomed.2019.03.035.

[12] Sun J, Jiang Y, Li L, Li R, Ling F, Du X, *et al*. HMGB-1/RAGE Signaling Regulates Th17/IL-17 and Its Role in Bronchial Epithelial-Mesenchymal Transformation. Current Molecular Medicine. 2024; 24: 1401–1412. https://doi.org/10.2174/0115665240249953231024060610.

[13] Chen J, Qin P, Sun Y, Han S. Histone lactylation promotes cell proliferation, migration and invasion through targeting HMGB-1 in endometriosis. Journal of Biomedical Research. 2023; 37: 470–478. https://doi.org/10.7555/JBR.37.20230095.

[14] Yi C, Zhang X, Li H, Chen G, Zeng B, Li Y, *et al*. EPHB4 Regulates the Proliferation and Metastasis of Oral Squamous Cell Carcinoma through the HMGB-1/NF-κB Signalling Pathway. Journal of Cancer. 2021; 12: 5999–6011. https://doi.org/10.7150/jca.59331.

[15] Liu M, Lu J, Zhang Q, Zhang Y, Guo Z. Clara cell 16 KDa protein mitigates house dust mite-induced airway inflammation and damage via regulating airway epithelial cell apoptosis in a manner dependent on HMGB-1-mediated signaling inhibition. Molecular Medicine (Cambridge, Mass.). 2021; 27: 11. https://doi.org/10.1186/s10020-021-00277-4.

[16] Andersson U, Tracey KJ, Yang H. Post-Translational Modification of HMGB-1 Disulfide Bonds in Stimulating and Inhibiting Inflammation. Cells. 2021; 10: 3323. https://doi.org/10.3390/cells10123323.

[17] Xu Y, Chen F. Antioxidant, Anti-Inflammatory and Anti-Apoptotic Activities of Nesfatin-1: A Review. Journal of Inflammation Research. 2020; 13: 607–617. https://doi.org/10.2147/JIR.S273446.

[18] Cheng H, Zhu Y, Chen L, Wang Y. Nesfatin-1 alleviated lipopolysaccharide-induced acute lung injury through regulating inflammatory response associated with macrophages modulation. Journal of Cardiothoracic Surgery. 2022; 17: 206. https://doi.org/10.1186/s13019-022-01952-1.

[19] Yang X, Jin Z, Wang X, Wu J, Yu W, Yao S, *et al*. Nesfatin-1 alleviates hyperoxia-induced lung injury in newborn mice by inhibiting oxidative stress through regulating SIRT1/PGC-1α pathway. Cytokine. 2023; 169: 156239. https://doi.org/10.1016/j.cyto.2023.156239.

[20] Atochina-Vasserman EN, Abramova E, James ML, Rue R, Liu AY, Ersumo NT, *et al*. Pharmacological targeting of VEGFR signaling with axitinib inhibits Tsc2-null lesion growth in the mouse model of lymphangioleiomyomatosis. American Journal of Physiology. Lung Cellular and Molecular Physiology. 2015; 309: L1447–L1454. https://doi.org/10.1152/ajplung.00262.2015.

[21] Tang Y, Liu J, Liu L. Angiotensin-converting Enzyme 2 Suppresses Pulmonary Fibrosis Associated with Wnt and TGF-β1 Signaling Pathways. Discovery Medicine. 2024; 36: 2274–2286. https://doi.org/10.24976/Discov.Med.202436190.209.

[22] Philpot P, Graumuller F, Melchiorre N, Prahaladan V, Takada X, Chandran S, *et al*. Hyperoxia-Induced miR-195 Causes Bronchopulmonary Dysplasia in Neonatal Mice. Biomedicines. 2024; 12: 1208. https://doi.org/10.3390/biomedicines12061208.

[23] Geetha O, Rajadurai VS, Anand AJ, Dela Puerta R, Huey Quek B, Khoo PC, *et al*. New BPD-prevalence and risk factors for bronchopulmonary dysplasia/mortality in extremely low gestational age infants ≤28 weeks. Journal of Perinatology: Official Journal of the California Perinatal Association. 2021; 41: 1943–1950. https://doi.org/10.1038/s41372-021-01095-6.

[24] Holzfurtner L, Shahzad T, Dong Y, Rekers L, Selting A, Staude B, *et al*. When inflammation meets lung development-an update on the pathogenesis of bronchopulmonary dysplasia. Molecular and Cellular Pediatrics. 2022; 9: 7. https://doi.org/10.1186/s40348-022-00137-z.

[25] Heydarian M, Schulz C, Stoeger T, Hilgendorff A. Association of immune cell recruitment and BPD development. Molecular and Cellular Pediatrics. 2022; 9: 16. https://doi.org/10.1186/s40348-022-00148-w.

[26] Zou S, Jie H, Han X, Wang J. The role of neutrophil extracellular traps in sepsis and sepsis-related acute lung injury. International Immunopharmacology. 2023; 124: 110436. https://doi.org/10.1016/j.intimp.2023.110436.

[27] Sun L, Zhang M, Jiang J, Liu W, Zhao W, Li F. Neutrophil extracellular traps promote bronchopulmonary dysplasia-like injury in neonatal mice *via* the WNT/β-catenin pathway. Frontiers in Cellular and Infection Microbiology. 2023; 13: 1126516. https://doi.org/10.3389/fcimb.2023.1126516.

[28] Dömer D, Walther T, Möller S, Behnen M, Laskay T. Neutrophil Extracellular Traps Activate Proinflammatory Functions of Human Neutrophils. Frontiers in Immunology. 2021; 12: 636954. https://doi.org/10.3389/fimmu.2021.636954.

[29] Sikora JP, Karawani J, Sobczak J. Neutrophils and the Systemic Inflammatory Response Syndrome (SIRS). International Journal of Molecular Sciences. 2023; 24: 13469. https://doi.org/10.3390/ijms241713469.

[30] Zhao X, Zhang L, Liu X, Zhao Z, Zhong X, Wang Y. Exogenous hydrogen sulfide inhibits neutrophils extracellular traps formation via the HMGB-1/TLR4/p-38 MAPK/ROS axis in hyperhomocysteinemia rats. Biochemical and Biophysical Research Communications. 2021; 537: 7–14. https://doi.org/10.1016/j.bbrc.2020.12.059.

[31] Wang S, Zhang Y. HMGB-1 in inflammation and cancer. Journal of Hematology & Oncology. 2020; 13: 116. https://doi.org/10.1186/s13045-020-00950-x.

[32] Okuma Y, Becker LB, Hayashida K, Aoki T, Saeki K, Nishikimi M, *et al*. Effects of Post-Resuscitation Normoxic Therapy on Oxygen-Sensitive Oxidative Stress in a Rat Model of Cardiac Arrest. Journal of the American Heart Association. 2021; 10: e018773. https://doi.org/10.1161/JAHA.120.018773.

[33] Yang Q, Li M, Hou Y, He H, Sun S. High-mobility group box 1 emerges as a therapeutic target for asthma. Immunity, Inflammation and Disease. 2023; 11: e1124. https://doi.org/10.1002/iid3.1124.

[34] Shi S, Chen Y, Luo Z, Nie G, Dai Y. Role of oxidative stress and inflammation-related signaling pathways in doxorubicin-induced cardiomyopathy. Cell Communication and Signaling: CCS. 2023; 21: 61. https://doi.org/10.1186/s12964-023-01077-5.

[35] Zhang H, Liu H. Mechanism of Weiwei granules in the treatment of chronic active *Helicobacter pylori* gastritis with atrophy based on the TLR4/NF-κB/COX-2 inflammatory signaling pathway. Histology and Histopathology. 2024; 39: 761–769. https://doi.org/10.14670/HH-18-679.

[36] Qi HM, Cao Q, Liu Q. TLR4 regulates vascular smooth muscle cell proliferation in hypertension via modulation of the NLRP3 inflammasome. American Journal of Translational Research. 2021; 13: 314–325.